The Meteoritical Society

Meteoritics & Planetary Science 53, Nr 1, 50–61 (2018)
doi: 10.1111/maps.13000

Liebermannite, $KAlSi_3O_8$, a new shock-metamorphic, high-pressure mineral from the Zagami Martian meteorite

Chi MA[1,*], Oliver TSCHAUNER[2], John R. BECKETT[1], George R. ROSSMAN[1], Clemens PRESCHER[3], Vitali B. PRAKAPENKA[3], Hans A. BECHTEL[4], and Alastair MACDOWELL[4]

[1]Division of Geological and Planetary Sciences, California Institute of Technology, Pasadena, California 91125, USA
[2]High Pressure Science and Engineering Center and Department of Geoscience, University of Nevada, Las Vegas, Nevada 89154, USA
[3]Center of Advanced Radiation Sources, GSECARS, The University of Chicago, Chicago, Illinois 60632, USA
[4]Advanced Light Source, ESG, Lawrence Berkeley National Laboratory, Berkeley, California 94720, USA
[*]Corresponding author. E-mail: chi@gps.caltech.edu

(Received 21 February 2017; revision accepted 30 September 2017)

Abstract–In this paper, we discuss the occurrence of liebermannite (IMA 2013-128), $KAlSi_3O_8$, a new, shock-generated, high-pressure tetragonal hollandite-type structure silicate mineral, in the Zagami basaltic shergottite meteorite. Liebermannite crystallizes in space group $I4/m$ with $Z = 2$, cell dimensions of $a = 9.15 \pm 0.14$ (1σ) Å, $c = 2.74 \pm 0.13$ Å, and a cell volume of 229 ± 19 Å^3 (for the type material), as revealed by synchrotron diffraction. In Zagami, liebermannite likely formed via solid-state transformation of primary igneous K-feldspar during an impact event that achieved pressures of ~20 GPa or more. The mineral name is in honor of Robert C. Liebermann, a high-pressure mineral physicist at Stony Brook University, New York, USA.

INTRODUCTION

Basaltic shergottites provide key insights into igneous processes on Mars (e.g., McSween 1994; Bridges and Warren 2006) but they are also highly shocked (Fritz et al. 2005), thereby providing information about shock conditions during the excavation of samples from the planet and of shock processes in general (e.g., Stöffler et al. 1991; Sharp and DeCarli 2006; Beck et al. 2007). Shocked meteorites are also the main source of natural samples of high-pressure minerals (e.g., Binns et al. 1969; Smith and Mason 1970; Price et al. 1983; Sharp et al. 1997; Tomioka and Fujino 1999; Tschauner et al. 2014; Walton et al. 2014; Ma et al. 2015b, 2016, 2017), many of which are rock-forming in the deep Earth or important carriers of incompatible elements (e.g., Stixrude and Lithgow-Bertelloni 2012; Kawai and Tsuchiya 2013).

Silicate hollandites are of particular interest because of their affinity for large, low-valence cations. This affinity is the result of a structure consisting of edge-sharing octahedra that form chains parallel to the *c* axis and are corner-linked to form cavities containing K and other large cations (Byström and Byström 1950). It also makes hollandites potentially important carriers of large ion lithophile elements in the Earth's mantle and, hence, important contributors to the Earth's heat budget (Zhang et al. 1993; Yagi et al. 1994; Harlow and Davies 2004; Ferroir et al. 2006). Lingunite, $NaAlSi_3O_8$ in the hollandite-type structure, named and approved as a new mineral (IMA 2004-054; Liu and El Goresy 2007), has been observed in ordinary chondrites (e.g., Gillet et al. 2000; Kimura et al. 2003). Here, we report the occurrence of liebermannite, $KAlSi_3O_8$ in the tetragonal hollandite-type structure observed in the Martian shergottite Zagami, and on the implications of this new high-pressure silicate for the Zagami impact event.

Natural occurrences of liebermannite were previously described by Langenhorst and Poirier (2000) and Beck et al. (2005, 2007) in the basaltic shergottites Zagami and Northwest Africa (NWA) 480. These authors characterized the phase using analytical transmission electron microscopy and electron probe microanalysis in combination with Raman spectroscopy. However, no quantitative structural analysis was presented. The present work represents the first report

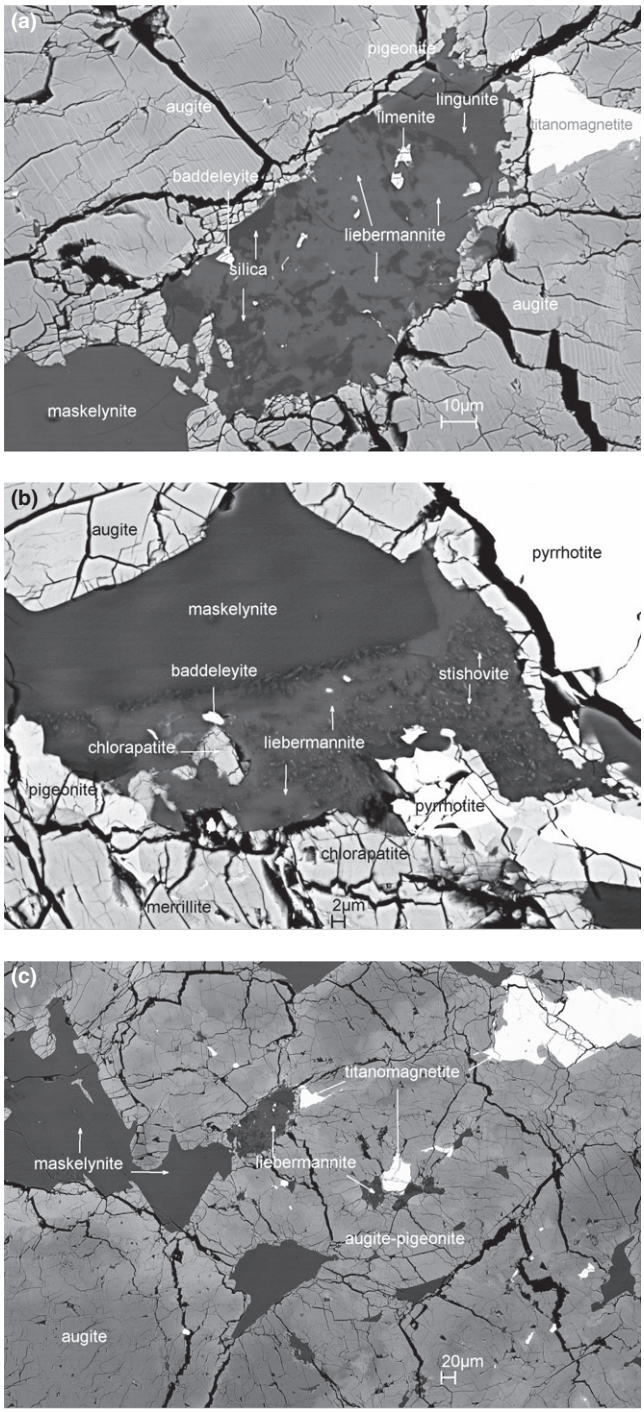

Fig. 1. BSE images of Zagami USNM 7619. a) First occurrence of liebermannite, which occurs with lingunite, a silica phase, ilmenite, and baddeleyite; the assemblage is surrounded by augite and pigeonite with nearby maskelynite and titanomagnetite. This is the type material for liebermannite. b) The second occurrence of liebermannite, with silica, chlorapatite and baddeleyite, bounded by augite, pigeonite, chlorapatite, maskelynite, and pyrrhotite. The patchy appearance in terms of grayscale contrast in maskelynite is an artifact, derived from high-current BSE imaging (at 15 kV and 5 nA). c) The third occurrence of liebermannite, which is ~140 μm away from the type material shown in panel a.

of liebermannite as a mineral approved by the Commission on New Minerals, Nomenclature and Classification of the International Mineralogical Association (IMA 2013-128) (Ma et al. 2014a). The name liebermannite honors the mineral physicist Robert Liebermann of Stony Brook University for his many contributions to the experimental study of phases at elevated pressures and temperatures (e.g., Liebermann 1970, 2014). Ma et al. (2014b, 2015a) provided preliminary reports on the results of this study.

SAMPLE AND METHODS

The Zagami meteorite, which fell at Zagami, Katsina Province, Nigeria on October 3, 1962, is a Martian-enriched basaltic shergottite (e.g., Bridges and Warren 2006) with abundant black shock veins (e.g., McCoy et al. 1992). It is one of only five Martian meteorite falls (versus ~100 Martian meteorite finds). The type material of liebermannite, identified in a Caltech Zagami thin section (Fig. 1), has been deposited in the collections of the Smithsonian Institution's National Museum of Natural History, Washington, DC, USA, under registration number USNM 7619.

Electron probe microanalysis (EPMA), high-resolution scanning electron microscope (SEM), electron backscatter diffraction (EBSD), synchrotron X-ray diffraction, and micro-Raman analyses were used to characterize the specimen. Backscattered electron (BSE) imaging was performed using a Carl Zeiss, LLC 1550VP field emission SEM. The EBSD analyses were performed using an HKL EBSD system on the ZEISS 1550VP SEM. Chemical analyses were performed with a JEOL 8200 electron microprobe (WDS: 15 kV, 5 nA, beam in focused mode) interfaced with the Probe for EPMA program from Probe Software, Inc. Standards for analysis were Asbestos microcline (Si$K\alpha$, Al$K\alpha$, K$K\alpha$), synthetic anorthite (Ca$K\alpha$), Amelia albite (Na$K\alpha$), synthetic fayalite (Fe$K\alpha$), synthetic forsterite (Mg$K\alpha$), synthetic TiO_2 (Ti$K\alpha$), synthetic Cr_2O_3 (Cr$K\alpha$), and synthetic Mn-olivine (Mn$K\alpha$). Counting times were 20 s on-peak and 10 s each on high and low background positions. Quantitative elemental microanalyses were processed with the CITZAF correction procedure (Armstrong 1995) and analytical results are given in Table 1. The detection limits (wt%) are 0.05 Si, 0.04 Ti, 0.06 Al, 0.06 Fe, 0.02 Mg, 0.02 Ca, 0.03 Na, 0.02 K, 0.05 Cr, and 0.06 Mn. The accuracy is 1–2% for Si, Al, Ca, Na, and K, based on analysis of feldspar standards as unknowns.

Table 1. Analytical data for liebermannite and associated lingunite and maskelynite.

Oxide	Type liebermannite[a] $n = 6$[b]	The second liebermannite[a] $n = 2$	The third liebermannite[a] $n = 3$	Lingunite next to type liebermannite $n = 3$	Maskeleyite near type liebermannite $n = 5$	Maskeleyite near the 2nd liebermannite $n = 4$
SiO_2	65.4 (0.3)[c]	68 (2)	66 (2)	59.3 (0.8)	57.1 (0.7)	59.6 (0.2)
TiO_2	b.d.[d]	0.09 (0.06)	0.06 (0.02)	b.d.	0.07 (0.05)	0.09 (0.02)
Al_2O_3	19.0 (0.2)	19.8 (0.4)	20 (1)	26.0 (0.2)	26.5 (0.5)	26.3 (0.3)
FeO	b.d.	0.30 (0.03)	0.35 (0.04)	b.d.	0.66 (0.04)	0.73 (0.08)
CaO	0.37 (0.09)	1.4 (0.7)	1.5 (0.3)	7.9 (0.3)	9.0 (0.4)	7.9 (0.2)
Na_2O	1.62 (0.04)	2.2 (0.3)	2.1 (0.5)	6.0 (0.1)	5.8 (0.2)	5.5 (0.2)
K_2O	13.02 (0.09)	8.53 (0.06)	11 (1)	0.4 (0.02)	0.41 (0.05)	0.75 (0.02)
Total	99.4	100.3	101.0	99.6	99.5	100.9
No. O atoms	8	8	8	8	8	8
Si	3.00	3.01	2.95	2.65	2.58	2.64
Ti		0.00	0.00		0.00	0.00
Al	1.03	1.04	1.07	1.37	1.41	1.37
Fe		0.01	0.01		0.03	0.03
Ca	0.02	0.07	0.07	0.38	0.43	0.37
Na	0.14	0.19	0.19	0.52	0.50	0.47
K	0.76	0.48	0.60	0.02	0.02	0.04
Sum cations	4.95	4.80	4.89	4.94	4.97	4.92

[a]See caption to Fig. 1 for explanation of terms.
[b]n = number of analyses.
[c]Errors given inside parentheses are one standard deviation of the mean based on all of the analyses.
[d]b.d. = below detection limit. Magnesium, Cr, and Mn were also analyzed but were below the detection limit in all cases.

Synchrotron diffraction data were collected at beamline 12.2.2, Advanced Light Source (ALS), Lawrence Berkeley National Laboratory, using a primary beam energy of 25.000 keV (0.49594 Å) monochromatized by a double crystal Si 111 monochromator. The X-ray beam was focused to a 20×15 μm^2 area by vertical and horizontal Kirkpatrick–Baez mirrors, and diffraction data were then collected using a MAR 345 image plate detector with φ as the only physical axis of rotation over 80°, taken in 1° increments. Additional data were obtained at beamline 13-IDD, GSECARS, Advanced Photon Source (APS), Argonne National Laboratory, which was run using a primary beam energy of 40.000 keV focused to a 3×4 μm^2 area and a Rayonix MAR 165 CCD area detector.

Raman spectra of liebermannite, silica, and lingunite were obtained using a 514.3 nm solid-state laser in a Renishaw M1000 micro-Raman spectrometer system with a spot size of ~2 μm. The methods were described in Ma and Rossman (2008, 2009). We collected numerous spectra on occurrences of liebermannite and lingunite in USNM 7619 using various approaches (e.g., various laser powers, focused and defocused beams, variable counting times) but all of the spectra were featureless. In contrast, Raman spectra of surrounding augite and pigeonite and of synthetic pure liebermannite were well defined. We discuss the reasons for the lack of detectable Raman shifts in natural type liebermannite below.

IR reflectance spectra of synthetic and natural liebermannite were obtained at beamline 5.4 at the Advanced Light Source, Berkeley, using a mercury-cadmium telluride detector, KBr beamsplitter, 0.48 cm^{-1} resolution and 10×14 μm^2 spatial resolution. Data were collected in mapping mode with a grid. Raman and IR-spectra were calculated with a force constant model (Dowty 1987) using force constants obtained by fitting the Raman spectra of stishovite and synthetic liebermannite.

RESULTS

Occurrence

The Zagami thin section (USNM 7619) is dominated by augite, pigeonite, and maskelynite, with minor mesostasis and accessory silica, merrillite, apatite, fayalite, ilmenite, titanomagnetite, baddeleyite, and pyrrhotite. The basic petrography is consistent with an NZ ("normal Zagami") lithology (Stolper and McSween 1979; McCoy et al. 1992). Shock melt pockets and veins are volumetrically minor in USNM 7619 (a relatively small thin section, 6×10 mm^2) and we observed only one of each. Thus, high-pressure phase assemblages,

which are typically associated with shock melt veins and pockets, occur heterogeneously; shock phases that we observed in USNM 7619 include stishovite, lingunite, liebermannite (as discussed in this paper), maskelynite, a high-pressure, calcium-aluminosilicate phase, zagamiite (Ma and Tschauner 2017; Ma et al. 2017), and a new type of tissintite (Ma and Beckett 2017). Seifertite has also been reported (El Goresy et al. 2008). Literature descriptions of shock-metamorphic phases in Zagami can be found in Beck et al. (2004, 2005), Langenhorst and Poirier (2000), and Malavergne et al. (2001).

A first occurrence of liebermannite was observed with lingunite, silica, ilmenite, and baddeleyite, surrounded by augite-pigeonite with nearby maskelynite and titanomagnetite (Fig. 1a; this is the type material). A second occurrence of liebermannite is associated with silica, chlorapatite, and baddeleyite (Fig. 1b). A third occurrence is shown in Fig. 1c, close to the type occurrence. Liebermannite in Zagami is colorless and transparent in plane light, occurring in aggregates up to 15 μm across within regions of 1000–4000 μm^2. In the type occurrence (Fig. 1a), individual crystallites are 2–10 μm in diameter; grains are smaller, 1 μm diameter or less, in the second occurrence (Fig. 1b), where they form textured aggregates, as revealed by synchrotron diffraction.

According to Stolper and McSween (1979), K-rich mesostases are more reddish in plane polarized light than K-poor mesostases. Reconnaissance tests confirm their observation for reddish K-rich mesostases (including K-feldspar composition domains) in our section, and in none of these examples was the material very prone to beam damage. Only two (K-rich) liebermannite occurrences (Figs. 1a and 1b) were established using synchrotron diffraction but both are optically transparent and colorless (i.e., not red) and both are highly sensitive to electron beam damage. It may, therefore, be possible to identify liebermannite-bearing regions in Zagami through the simple artifice of connecting K-mapping by EPMA to determine the locations of K-enriched regions and using optical properties and sensitivity to beam damage to determine which of these contain liebermannite. We designated the third occurrence of liebermannite, shown in Fig. 1c, based on electron beam sensitivity and because it was transparent in plane light.

Chemical Composition and Crystallography

The compositions of liebermannite, lingunite, and nearby maskelynite determined by EPMA are given in Table 1. The composition of type liebermannite leads to a formula of $(K_{0.76}Na_{0.14}Ca_{0.02})Al_{1.03}Si_{3.00}O_8$ and a density of 3.98 g cm^{-3} using the cell parameters described below from synchrotron diffraction. Although a low beam current of 5 nA was used for the analysis, the low cation sum (0.92) for the K-site is likely due to diffusion of Na away from the electron beam. Aluminum and Si contents are consistent with full occupancy of the K-site by monovalent cations. The endmember formula of liebermannite is $KAlSi_3O_8$, which requires SiO_2 64.76, Al_2O_3 18.32, and K_2O 16.92 (total 100.00 wt%). Observed K/Na atomic ratios range from 2.53 to 5.43, and all of the liebermannite crystals have significant amounts of Ca (0.02–0.07 pfu).

We were unable to obtain EBSD patterns on Zagami liebermannite, and Raman spectra were featureless. Given the results described below, we infer that EBSD failed to produce viable patterns for liebermannite because the examined crystallites were both electron beam-sensitive and highly deformed. Damage marks generated by a focused electron beam were observed during EBSD analysis. High-pressure phases in shocked meteorites are often beam-sensitive, so the possibility that this was a high-pressure polymorph of $KAlSi_3O_8$ led us to examine the sample using synchrotron diffraction, which is much less damaging.

Synchrotron diffraction revealed the crystal structure of liebermannite. The type material in Fig. 1a, examined at ALS, gave rise to a set of broad single crystal reflections with 3–5° full width at half maximum (FMHW) along the φ- and *x*-axes (the *x*-axis being the azimuthal angle within the detector plane) (Fig. 2a). The observed reflections are superimposed on a vitreous signal of maskelynite and occur in the center of a dense region that lies on the top of the maskelynite. Using the RSV program (Dera et al. 2013), we identified within this set of reflections two subsets of 20 and 21 reflections, each of which belonged to a reciprocal lattice. Indexing these sets individually with Cellnow and Xprepr (Sheldrick 2008a, 2008b) gave tetragonal or pseudotetragonal cells with dimensions of 9.0–9.4 Å for two and 2.6–2.7 Å for the third axis, and angles of 90°±0.5°. All cells were compatible with body-centered Bravais lattices. Initially, we left open the question whether this crystalline phase assumes a tetragonal or a pseudotetragonal metric, as both tetragonal and monoclinic cells were compatible with the observed set of reflections. We note that the compatible monoclinic cells match by Bravais type and cell shape the direct subgroups of the tetragonal body-centered cell in space group $I4/m$. Regardless of the space group, however, the cell dimensions imply a density of ~4 g cm^{-3} for the following reasons. The chemical formula $(K,Na)AlSi_3O_8$ implies that the site with lowest Wyckhoff multiplicity is occupied by the alkali atoms. The multiplicity of this site is 2 (in both the tetragonal and monoclinic cells

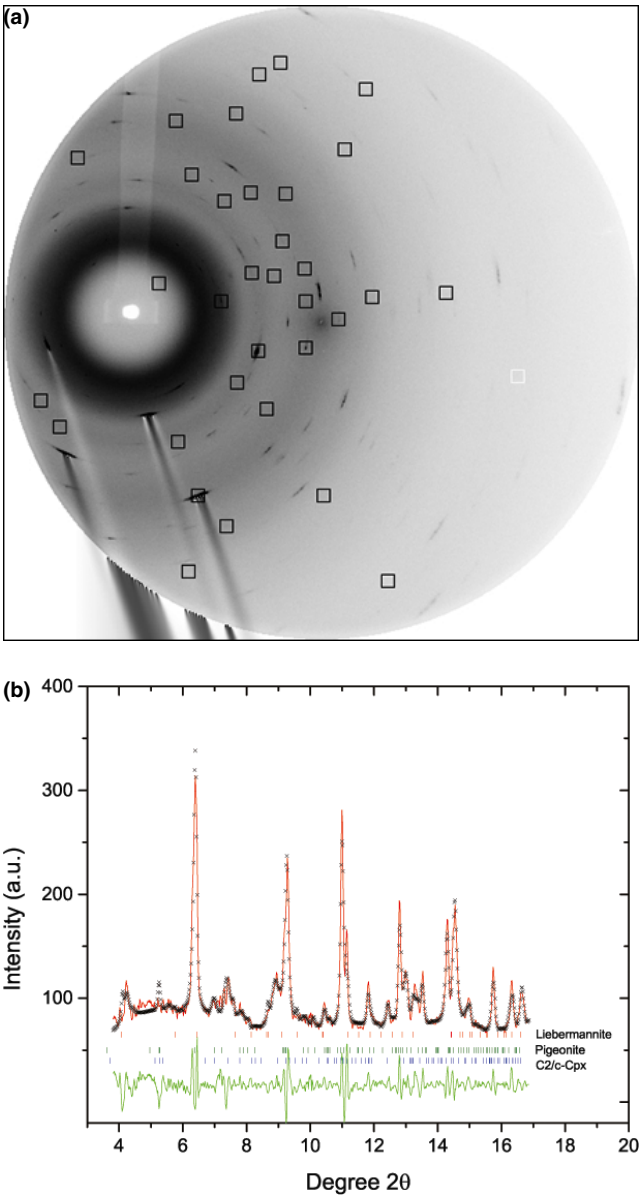

Fig. 2. a) Wide sweep diffractogram of liebermannite reflections from the type material. The diffraction signal was obtained during rotation along the ω-axis of the goniometer. Reflections of liebermannite are from two or three multidomain crystals that exhibit substantial deformation. The high level of deformation is apparent in the large rocking curve of the reflections along the *x*-axis (the in-plane azimuthal angle in the given geometry). Black boxes indicate the locations of reflections from the merged set of two crystal domains, which were used for structure analysis. This set of reflections was used for structure identification. Data were collected at the beamline 12.2.2 ALS with a 0.4959 Å wavelength. Streak features are artifacts generated by intense reflections. b) Integrated diffraction pattern (black crosses) and modeled diffraction pattern (red curve in online version) from Rietveld refinement of liebermannite in the second occurrence along with coexisting clinopyroxene and pigeonite. The positions of prominent peaks for each phase are shown below the diffraction pattern. Differences between experimental and modeled patterns are shown at the bottom (green in online version). The volume fractions of the three minerals were 18, 48, and 34 vol% (±2%) for liebermannite, clinopyroxene, and pigeonite, respectively. Liebermannite exhibits marked texture that was fitted by spherical harmonics with the GSAS Rietveld refinement software. Pigeonite is from material underneath the shock-metamorphised mesostasis that contains fine-grained liebermannite and clinopyroxene. (Color figure can be viewed at wileyonlinelibrary.com.)

that are compatible with the data). The stoichiometry then requires that Si and Al reside together on one site with multiplicity of 8 or on two sites with multiplicity 4. Oxygen, accordingly, is located on two or four such sites. Thus, with the given unit cell dimensions, Z is 2 and the density must be approximately 4 g cm^{-3}, irrespective of the detailed crystal structure.

In summary, we detected a crystalline phase of composition (K,Na)$AlSi_3O_8$ with a density of ~4 g cm^{-3} and cell dimensions around $9 \times 9 \times 2.6$ Å^3. In addition, all unit cells match, by Bravais type and cell shape, the space group $I4/m$ or its direct monoclinic subgroup $I2/m$ ($C2/m$) in various settings. Hollandite-type $KAlSi_3O_8$ (Akaogi et al. 2004) is the only phase matching all of these constraints that is known from experiments within the K_2O-Al_2O_3-SiO_2 system for pressures below ~20 GPa. The tetragonal hollandite phase does transform to a monoclinic $I2/m$ structure at ~20 GPa but this transition is unquenchable in experiments (Ferroir et al. 2006).

We took an additional step in analyzing the structural data by examining the compatibility of the observed reflection intensities with the hollandite-type structure. We rescaled and combined the two sets of reflections, resulting in a set of 11 unique, merged reflections (i.e., averaged symmetry-equivalent reflections). The integral R-factor, which measures the deviation of observed symmetry-equivalent reflections from their average, does not indicate a preference for tetragonal or pseudotetragonal monoclinic cells. Hence, we use the more highly symmetric cell (i.e., tetragonal) as a basis for the structure model. Although the number of unique reflections is 11, the number of refinable parameters in the structure is 10 (fractional coordinates x/a and y/b for ions Si, O1, and O2 [Table 2], and B_{iso} of (K+Na), (Si+Al), O1, and O2). Given the sparse data set, we pursued the following approach. (1) We refined B_{iso} and the Al+Si site occupancies in Shelx (Sheldrick 2008a) and (2) we examined the overall compatibility of the structure and data using a reversed Monte Carlo approach, which measures the compatibility of different configurations of $K(Si,Al)_4O_8$ and $KAlSi_3O_8$ within the given unit cell shape without bias by crystal symmetry. We found convergence and goodness of fit for the hollandite-type structure of

Table 2. Atom coordinates of type liebermannite structure.

	x/a	*y/b*	*z/c*	Occ.	B_{iso}
K	0	0	0.5	0.76	0.65 (4)
Na	0	0	0.5	0.14	0.65 (4)
Ca	0	0	0.5	0.02	0.65 (4)
Si	0.346 (5)	0.15 (2)	0	0.657	0.47 (4)
Al	0.346 (5)	0.15 (2)	0	0.343	0.47 (4)
O1	0.20[a]	0.20[a]	0		0.14 (1)
O2	0.50[a]	0.16[a]	0		0.12 (3)

[a]Fixed.

Table 3. List of observed and calculated normalized structure factor moduli of unique reflections of type liebermannite in Fig. 1a.

h	*k*	*l*	Fo^2	Fc^2	$\sigma(F^2)/su$	*Fc/Fc* (max)	Resolution (Å)
4	4	0	64.12	143.93	1.95	0.146	1.62
6	10	0	9.47	0.01	1.42	0.001	0.78
1	5	0	1032.02	1198.46	1.2	0.421	1.79
0	6	0	500.57	414.17	1.05	0.247	1.52
0	3	1	7251.11	6766.4	1.04	1	2.04
−3	6	1	15.36	31.5	0.84	0.068	1.22
−3	5	0	166.15	134.63	0.69	0.141	1.57
−2	5	1	138.81	112.86	0.62	0.129	1.44
−1	5	0	1021.21	1090.94	0.51	0.402	1.79
5	7	0	11.18	14.4	0.24	0.046	1.06
1	4	1	269.15	278.55	0.15	0.203	1.72

$R_1 = 0.088$ for 11 unique reflections after merging for Fourier, $wR_2 = 0.1617$, GooF = S = 0.943.

$KAlSi_3O_8$: $R_1 = 0.09$, $wR_2 = 0.16$, GooF = S = 0.943, and we obtained $R_F = 0.06$ in the reversed Monte Carlo analysis. This analysis confirms that the observed reflections are highly compatible with hollandite-type (K, Na)$AlSi_3O_8$ (Table 3).

The symmetry-constrained cell refinement led to a tetragonal cell with $a = 9.15 \pm 0.14$ (1σ), $c = 2.74 \pm 0.13$ Å, and a cell volume of 229 ± 19 Å^3. Atomic coordinates are given in Table 2 and structure factor moduli in Table 3. The *a* cell dimension of 9.14 ± 0.14 Å is noticeably shorter but overlaps within uncertainties with values reported in the literature for synthetic and meteoritic Na/K-hollandites, which are ≥9.26 Å (Ringwood et al. 1967; Yamada et al. 1984; Zhang et al. 1993; Gillet et al. 2000; Langenhorst and Poirier 2000; Akaogi et al. 2004; Ferroir et al. 2006; Boffa Ballaran et al. 2009). In turn, the *c* axis is a bit larger but overlaps within uncertainties with values for synthetic samples (2.74 ± 0.13 versus ~2.73 Å) and, consequently, the cell volume is smaller than values obtained from experimental data (229 ± 19 versus 232–243 Å^3) but, within uncertainties, overlapping. The marked uncertainty in cell dimensions corresponds directly to the large rocking curves of the observed reflections and a high degree of residual deformation. The angles of peak centroids have larger uncertainties than very sharp reflections of an undeformed, defect-free crystal, and the variance of reciprocal lattice vectors reflects an overall deformation of the lattice. Most of this deformation does not reflect elastic strain. For example, if we take the average cell dimensions of the liebermannite-type material, the strain of the *a* axis (relative to pure synthetic liebermannite [Boffa Ballaran et al. 2009]) corresponds to an axial stress of 9 GPa and the *c* axis dimension to an axial stress of −5 GPa. It is not to be expected that a solid with a shear modulus of 90 GPa (Boffa Ballaran et al. 2009; Ferroir et al. 2006) could sustain such large anisotropic stresses at ambient pressure. We interpret this strain to be the result of inelastic deformation that occurred upon shock release, similar to the high strain levels observed in shocked olivines in meteorites that experienced high-grade shock metamorphism (e.g., Jeanloz 1980; Stöffler et al. 1991). We note that liebermannite-lingunite solid solutions exhibit a ferroelastic transition above 17 GPa (e.g., Ferroir et al. 2006; Boffa Ballaran et al. 2009; Kawai and Tsuchiya 2013). Thus, plastic yielding upon high stress during shock release is to be expected and the observed strong deformation of natural liebermannite is a plausible result. For endmember lingunite, this transition is not reported and, consistently, there are no reports of such strong deformation in meteoritic lingunites; the observed diffraction signal reflects much less strain.

We examined a second occurrence of liebermannite (Fig. 1b) at APS beamline 13-IDD. This sample is a fine-grained, highly textured aggregate with strain-broadened reflections. We evaluated the results based on the structure model obtained above from the type occurrence and a refinement of texture, which was fitted by spherical harmonics (GSAS) using orientation matrix angles fitted with GSA (Dera et al. 2013). The Rietveld refinement converged to an Rwp of 10% (Fig. 2b). LeBail extraction of structure factor moduli converged to 7%. Structure factor moduli, extracted and corrected for texture effects, gave an R_F of 17.8% (Table 4). The cell parameters are close to the limits of those found for the type example, with $a = 9.296(9)$ Å (versus 9.15 ± 0.14) and $c = 2.772(6)$ Å (versus 2.74 ± 0.13). This difference is unlikely to be a simple consequence of the differing compositions ($Or_{48}Ab_{46}An_6$ versus $Or_{76}Ab_{22}An_2$ for the type material), as the cell parameters vary weakly with Na/K (Yagi et al. 1994). The discrepancy may be owed in part to the large deformation of the type material unit cell. The unit cell parameters for this second occurrence are comparable

Table 4. Structure factor moduli for the second occurrence of liebermannite in Fig. 1b.

h	k	l	d [Å]	$\lvert F_{calc}\rvert$	$\lvert F_{exp}\rvert$	$D(\lvert F\rvert)$
−2	0	0	4.72	298.3	180.2	118.1
−2	−2	0	3.338	195.1	191	4.1
−3	−1	0	2.986	337	382.9	−45.9
−1	−3	0	2.986	593.9	655.9	−62
−1	0	−1	2.51	219.1	203.6	15.5
−4	0	0	2.36	412.5	333.3	79.2
−3	−3	0	2.225	36.8	16.2	20.6
−2	−1	−1	2.216	494.2	357.7	136.5
−1	−2	−1	2.216	54.2	6.3	47.9
−4	−2	0	2.111	19.1	9.9	9.2
−2	−4	0	2.111	345.5	331.5	14
−3	0	−1	2.006	457.7	344.1	113.6
−5	−1	0	1.852	287.5	245	42.5
−1	−5	0	1.852	395.3	318.9	76.4
−3	−2	−1	1.846	0.4	22.5	−22.1
−2	−3	−1	1.846	187.1	198.2	−11.1
−4	−1	−1	1.719	277.1	379.3	−102.2
−1	−4	−1	1.719	522	793.7	−271.7
−4	−4	0	1.669	40.9	30.6	10.3
−5	−3	0	1.619	93.9	127.9	−34
−3	−5	0	1.619	24.8	17.1	7.7
−6	0	0	1.574	696.3	584.7	111.6
−5	0	−1	1.529	279.3	269.4	9.9
−4	−3	−1	1.529	12.5	12.6	−0.1
−3	−4	−1	1.529	165.7	155.9	9.8
−6	−2	0	1.493	255.7	258.6	−2.9
−2	−6	0	1.493	89.7	94.6	−4.9
−5	−2	−1	1.454	488.8	402.7	86.1
−2	−5	−1	1.454	525.9	431.5	94.4
−7	−1	0	1.335	92.1	81.1	11
−5	−5	0	1.335	68.5	80.2	−11.7
−1	−7	0	1.335	388.4	342.3	46.1
−6	−1	−1	1.333	165.3	144.1	21.2
−1	−6	−1	1.333	21.3	19.8	1.5
−6	−4	0	1.309	173.5	228.8	−55.3
−4	−6	0	1.309	324.4	406.3	−81.9
0	0	−2	1.302	883.9	1000	−116.1
−5	−4	−1	1.283	662.1	684.7	−22.6
−4	−5	−1	1.283	363.7	355	8.7
−1	−1	−2	1.278	93.3	65.8	27.5
−2	0	−2	1.255	152.8	141.4	11.4
−7	−3	0	1.24	258.9	243.2	15.7
−3	−7	0	1.24	179.3	164	15.3
−6	−3	−1	1.238	141.9	148.6	−6.7
−3	−6	−1	1.238	127	134.2	−7.2
−2	−2	−2	1.213	97.4	135.1	−37.7
−7	0	−1	1.198	19.4	22.5	−3.1
−3	−1	−2	1.193	185.9	217.1	−31.2
−1	−3	−2	1.193	315.7	355	−39.3
−8	0	0	1.18	134.9	167.6	−32.7
−7	−2	−1	1.161	56.5	88.3	−31.8
−2	−7	−1	1.161	130.9	177.5	−46.6
−8	−2	0	1.145	136.4	191	−54.6
−2	−8	0	1.145	98.7	128.8	−30.1

to values cited in the literature, whereby c is longer. This leads to a cell volume (240 ± 3 Å^3) at the higher end of values reported by other workers for synthetic K-hollandites (Ringwood et al. 1967; Yamada et al. 1984; Zhang et al. 1993; Akaogi et al. 2004; Ferroir et al. 2006).

The Raman spectra of liebermannite and lingunite in USNM 7619 were featureless. This result stands in sharp contrast to the well-defined Raman spectra of calcic hollandite from NWA 856 presented by Beck et al. (2004), lingunites from ordinary chondrites (e.g., Gillet et al. 2000; Kimura et al. 2003), or synthetic endmember liebermannite, which has characteristic bands at 214, 288, 511, 544, 726, and 762 (Fig. 3a; this study) or at 211, 281, 411, 540, 620, and 760 cm^{-1} (Chen et al. 2004). However, liebermannite and lingunite in USNM 7619 and Zagami occur in a different setting than lingunite in NWA 856 and in various chondrites. In the latter, hollandite-type silicate appears to have formed at high temperature, if not from melt (Gillet et al. 2000). In the regions of USNM 7619 and Zagami that we examined, liebermannite occurs within maskelynite and forms comparatively large (i.e., a few to 10 μm diameter), highly deformed crystallites. The deformation reduces phonon lifetime, while a high density of defects induces a highly structured background through broadband fluorescence; both of these effects contribute to the lack of observable Raman shifts. Moreover, the surrounding maskelynite generates intense broadband fluorescence, which defeats collection of Raman spectra with a laser operating in continuous wave mode and a detector that integrates signal over seconds to minutes. Therefore, we collected IR reflectance data on liebermannite in Zagami. Figure 3b shows the IR reflectance data of liebermannite and surrounding maskelynite in comparison to the reflectance spectrum of synthetic pure liebermannite collected using the same instrument. Despite the strong broad reflectance band of maskelynite, it is quite clear that synthetic and natural liebermannite exhibit very similar spectral features. We note that the spectrum of synthetic liebermannite appears to be strongly direction-dependent (Fig. 3c). The spectra of the fine-grained outer region of the sample give different peak intensities from those collected in the coarse-grained interior, although both regions show only diffraction patterns of liebermannite.

Based on the spectrum of a more fine-grained section of the synthetic sample and the natural sample in Zagami, we can assign the observed bands by using Dowty's (1987) force constant model. The highest vibrational energy corresponds to the superposition of two doubly degenerate asymmetric stretching modes (along x and y) and the band around 700–800 cm^{-1} to a doubly degenerate symmetric stretching mode.

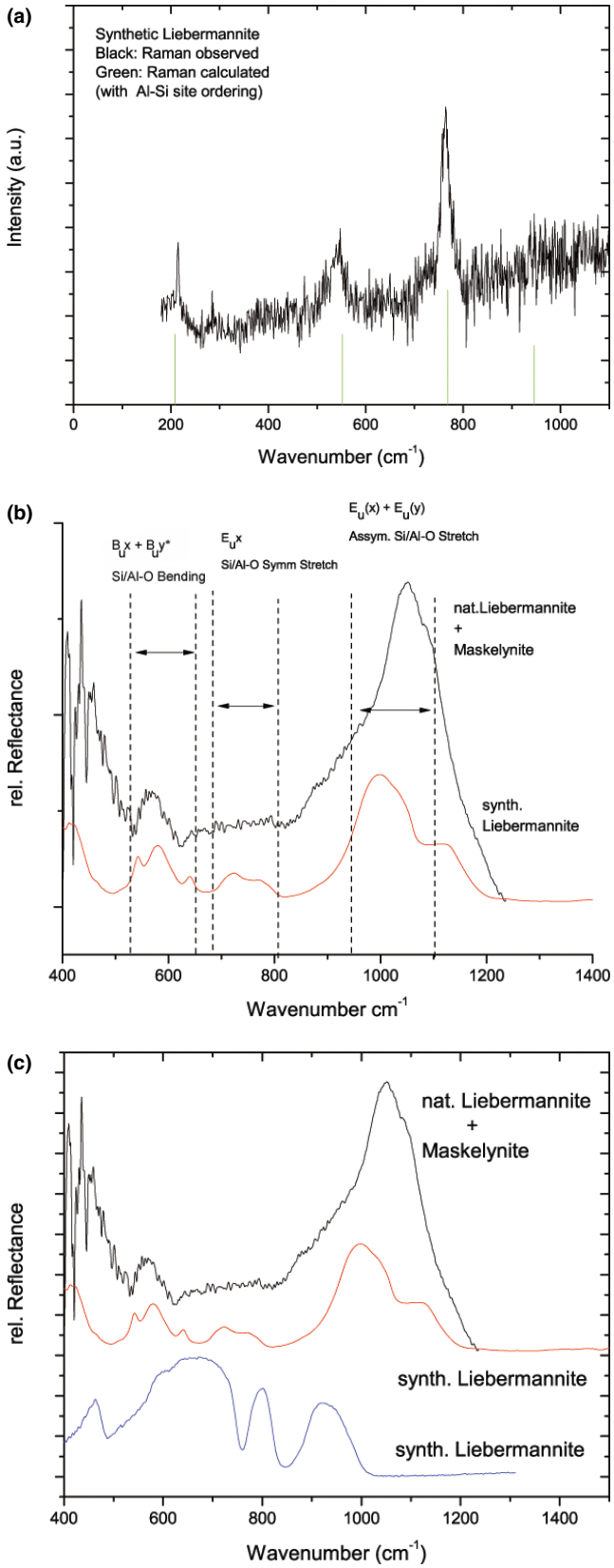

Fig. 3. a) Raman spectrum of synthetic liebermannite. Vertical lines (green in online version) indicate calculated energies of the Raman shifts of monoclinic liebermannite with Si and Al ordered. b) IR reflectance spectra of synthetic (upper) and natural (lower) liebermannite. Margins for calculated vibrational energies and mode assignments are indicated. The bands around 550–600 cm^{-1} do not occur as regular vibrations in tetragonal liebermannite. We modeled these bands by Al-Si site ordering and subsequent reduction of crystal symmetry to monoclinic. The star indicates that these mode assignments therefore do not refer to the same metric. Any of the sub-bands within the energy intervals 690–810 and 940–1200 cm^{-1} can also be interpreted as resulting from Si-Al ordering and symmetry reductions. c) IR reflectance spectra of natural (upper) and synthetic liebermannite (middle and lower) from different parts of the synthetic sample. The middle spectrum is from a fine-grained section and the lower one from a large grain of unknown orientation. Diffraction patterns show that both spectra adhere to liebermannite. It is possible that the coarser-grained section includes spectral features of organic material. (Color figure can be viewed at wileyonlinelibrary.com.)

Both Raman- and IR-spectra exhibit noticeable signals around 550–620 cm^{-1}. These features do not occur within any reasonable modification of force constants within Dowty's model as long as the main stretching vibrations remain matched. We observe that Si-Al site ordering with according symmetry reduction to $I2/m$ allows matching of all observed modes. We give the respective assignment in Fig. 3b (marked with a star) to indicate that the mode symmetry refers to a monoclinic rather than tetragonal metric. The other assignment refers to the tetragonal metric that we also used in the structure analysis. Our diffraction data cannot resolve a possible monoclinic symmetry reduction. Indeed, the diffraction pattern of synthetic liebermannite refines better with a monoclinic structure.

The high-energy shoulder in the reflectance band between 1000 and 1200 cm^{-1} in synthetic liebermannite is indicative of symmetry reduction through site ordering, as Al has lower mass than Si but similar bond distance and strength, and therefore an equivalent stretching vibration is shifted to higher energy. Figure 3a shows the Raman spectrum of synthetic liebermannite along with an indication of calculated mode energies using the monoclinic structure. We emphasize that the monoclinic symmetry reduction is not directly related to the known ferroelastic transition in silicate hollandites (Ferroir et al. 2006; Caracas and Boffa Ballaran 2010) but a consequence of Al-Si ordering. The Raman shift at 214 cm^{-1} corresponds to vibration of K atoms along the (pseudo-) fourfold axis.

Whether site ordering occurs during shock or release, or is induced by the probe laser-beam in the

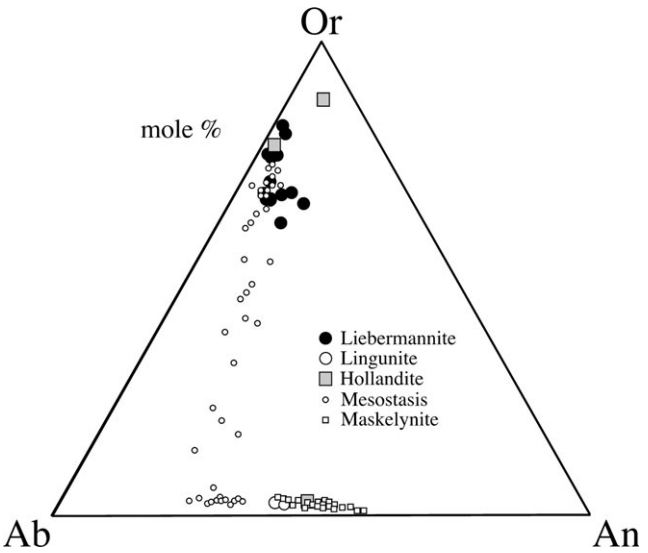

Fig. 4. Compositions of liebermannite and lingunite (this study); Na-K-Ca hollandites, labeled "Hollandite" (Langenhorst and Poirier 2000; Beck et al. 2007); mesostasis (Stolper and McSween 1979); and maskelynite (Stolper and McSween 1979; this study) from Zagami in terms of orthoclase–albite–anorthite molar abundances (Or-Ab-An). Compositions of liebermannite and lingunite from this study were modified from those given in Table 1 by adjusting Na contents to provide full occupancy of the K-site. Mesostasis compositions are projected from SiO_2 (i.e., a feldspar and the same feldspar but with an additional 2, 3, or 30 times as much quartz would plot in the same place).

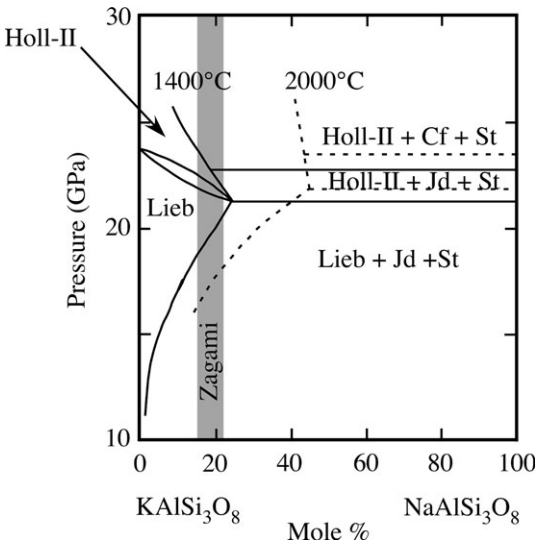

Fig. 5. Phase diagram for the $NaAlSi_3O_8$- $KAlSi_3O_8$ join at 1400 °C (solid curves and labeled fields) and 2000 °C (dashed) after Liu (2006) with compositions of Zagami liebermannite with <3 mole% An component from this study shaded in gray. Lieb = liebermannite; Holl-II = $I2/m$ hollandite; Jd = jadeite; Cf = Ca-ferrite structured $(Na,K)AlSiO_4$; St = stishovite. (Color figure can be viewed at wileyonlinelibrary.com.)

optical spectrometer, remains an open question. Al-Si site ordering can potentially be used to probe cooling rates in feldspar-bearing shock-metamorphic rocks and meteorites.

DISCUSSION

In this section, the conditions for liebermannite formation are evaluated by first considering associated phases in the studied sample. Figure 4 shows compositions of liebermannite and lingunite (the Na analog of liebermannite) from Zagami together with those of maskelynite and mesostasis (Stolper and McSween 1979) projected from SiO_2. Where projected from silica, liebermannite compositions are consistent with those of K-rich mesostasis compositions, which have silica in excess of the amount needed to construct feldspar; it is, therefore, likely that K-rich feldspars or feldspar composition glasses in mesostasis were the precursors to liebermannite. In contrast, reported lingunite compositions are substantially more calcic than K-poor mesostases; they plot with maskelynite in Fig. 4, making plagioclase, and not alkali feldspar in K-poor mesostasis, the likely precursor. If we accept a mesostasis origin for the liebermannite, then plagioclase coexisting with the original K-rich mesostasis would have been subjected to similar conditions.

The regions of Zagami containing liebermannite also contain maskelynite, stishovite, pigeonite, and lingunite (the hollandite-structured form of $NaAlSi_3O_8$). Stishovite is stable over a broad range of pressures and temperatures above 8–11 GPa (Mao et al. 2001). Maskelynite can also be formed under a variety of conditions (e.g., Fritz et al. 2005; Kubo et al. 2009; El Goresy et al. 2013). $NaAlSi_3O_8$, the endmember for lingunite, may not have a hollandite stability field at all (e.g., Deng et al. 2010) but meteoritic lingunites all have significant Ca contents and it is likely that Ca stabilizes them. Lingunites with compositions appropriate for meteoritic occurrences appear not to have been studied experimentally but they may provide important constraints on shock events because compositions of the meteoritic material are so restricted relative to the available range of bulk maskelynite and plagioclase precursors (Fig. 4).

Liebermannite exists stably over a broad range of pressures, temperatures, and bulk compositions (e.g., Yagi et al. 1994; Liu 2006; Boffa Ballaran et al. 2009), as shown in Fig. 5. At 1400 °C, low Ca-liebermannite plus stishovite (no pyroxene) of Fig. 1 would be stable at ~19–21 GPa, bounded at high pressure by the breakdown of liebermannite to a monoclinic $I2/m$ $(K,Na)AlSi_3O_8$ structure and, at low pressure, by the formation of pyroxene and stishovite. At higher

temperatures, the stability field expands toward both low (~17 GPa at 2000 °C) and, especially, high pressure.

Liebermannite in Zagami differs from most other known occurrences of high-pressure minerals in shocked meteorites by the comparatively large size of the crystallites and their high level of deformation. The 2–10 μm grains are large enough to generate single crystal diffraction patterns on the scale of microfocused X-ray beams, in contrast to the sub-μm grains of meteoritic ringwoodite, ahrensite, bridgmanite, akimotoite, and wadsleyite (Tschauner et al. 2014; Ma et al. 2016). High-pressure minerals in shock melt pockets and veins do not exhibit marked deformation indicating that, upon release from the shock state, the plastic limit was crossed at lower particle velocities than for liebermannite. We are also aware of one example of μm-scale crystallites formed in shock experiments. Asimow et al. (2016) observed the formation of Al-Fe-Cu quasicrystals far from the experimentally generated hot spot. The growth of these crystallites probably occurred upon release, because lattice deformation is very small (Asimow et al. 2016). In contrast, the deformation for Zagami liebermannite is large. As a rough approximation, we can estimate the dynamic stress that generated this deformation through the observed strain and known axial compressibilities to be $\sigma_{ii} = c_{iijj}\varepsilon_{jj} = (9 + 9 - 5)/3 = \sim 4$ GPa. This value then corresponds to a lower limit of the average stress bound for plastic deformation of liebermannite, although the large anisotropy in deformation indicates the likely relevance of directional stresses. The stress distribution and evolution upon shock release in the solid state is not homogeneous and, in the absence of what would be a very difficult, 3-D modeling of the release path in a polycrystalline aggregate, 4 GPa represents a zeroth order estimate of the plastic deformation limit. We note that this limit is rather low for a silicate or any material with a bulk modulus around 200 GPa and a shear modulus of 90 GPa (Ferroir et al. 2006; Boffa Ballaran et al. 2009). For instance, the Hugoniot elastic limit of olivine is around 12 GPa (Jackson and Ahrens 1979) and that of copper is 10 GPa (see for instance An et al. 2008).

The large grain size of liebermannite crystallites in Zagami suggests formation during shock or upon shock release through a mechanism different from formation of the high-pressure phases in melt pockets or veins (or the immediate vicinity thereof). Plausibly, this different mechanism is a solid-state transformation of precursor alkali feldspar to the high-pressure liebermannite structure. The highly deformed nature of the liebermannite crystals reflects anisotropic stresses during shock release. If pressures exceeded the stability of liebermannite and an $I2/m$ phase was produced, then back-transformation to $I4/m$ liebermannite occurred during quench, and anisotropic stresses shifted the transformation boundary to a lower average pressure range. The absence of jadeite in liebermannite-bearing aggregates, even for the relatively sodic compositions of the second occurrence, suggests relatively low formation temperatures (i.e., well below 2000 °C and likely below 1400 °C) with pressures of ~20 GPa or lower, although peak shock pressures could have been higher. The heat source for liebermannite occurrences shown in Fig. 1 is uncertain, because shock melt in USNM 7619 is >800 μm away from the liebermannite occurrences described here, at least in the two dimensions provided by the thin section. It is possible that a melt pocket or vein out of the plane of the section provided the heat source. Alternatively, small-scale cracks or voids in or near mesostasis collapsed during shock, leading to ~200 μm hot spots (e.g., Walton et al. 2014; Ma et al. 2016) that heated them enough to facilitate the formation of stishovite and/or silica glass plus liebermannite.

CONCLUDING REMARKS

Liebermannite is a new high-pressure form of $KAlSi_3O_8$, first observed in the Zagami basaltic shergottite from Mars, where it forms heterogeneously in K-rich mesostases after alkali feldspar. The large grain size and highly deformed nature of liebermannite type material suggest formation through a solid-state transformation, which may have occurred directly from alkali feldspar or as a back-transformation from a higher pressure phase during quench. The presence and composition of liebermannite and the presence or absence (as in Zagami) of an associated breakdown phase, jadeite, are key markers for shock conditions in such Martian meteorites. It is possible to identify liebermannite-bearing regions in Zagami through the simple artifice of connecting K-mapping by EPMA to determine the locations of K-enriched regions and using optical properties and sensitivity to beam damage to determine which of these areas contain liebermannite.

Acknowledgments—SEM, EBSD, EPMA, and Raman measurements were carried out at the Geological and Planetary Science Division Analytical Facility at Caltech, which is supported in part by NSF grants EAR-0318518, EAR-1322082, and DMR-0080065. This work was supported in part by the National Nuclear Security Administration under the Stewardship Science Academic Alliances program through DOE Cooperative Agreement #DE-NA0001982 and DESC0005278. This work was also supported by NASA grant NNX12AJ01G. The polished thin section of Zagami used in this study was kindly provided by E. M. Stolper. Part of this work was performed at GeoSoilEnviroCARS (Sector 13),

Advanced Photon Source (APS), Argonne National Laboratory. GeoSoilEnviroCARS is supported by NSF-EAR-1128799 and DE-FG02-94ER14466. The Advanced Photon Source, a DOE Office of Science User Facility, is operated by Argonne National Laboratory under Contract No. DE-AC02-06CH11357. The Advanced Light Source is supported by the Director, Office of Science, Office of Basic Energy Sciences, of the U.S. Department of Energy under Contract No. DE-AC02-05CH11231. We gratefully acknowledge Gabriel Gwanmesia and Baosheng Li for synthetic liebermannite. We thank Erin Walton, an anonymous reviewer, and AE Wolf Uwe Reimold for their constructive reviews.

Editorial Handling—Dr. W. Uwe Reimold

REFERENCES

Akaogi M., Kamii N., Kishi A., and Kojitani H. 2004. Calorimetric study of high-pressure transitions in $KAlSi_3O_8$. *Physics and Chemistry of Minerals* 31:85–91.

An Q., Luo S.-N., Han L.-B., Zheng L., and Tschauner O. 2008. Melting of Cu under hydrostatic and shock wave loading to high pressures. *Journal of Physics: Condensed Matter* 20:8.

Armstrong J. T. 1995. CITZAF—A package of correction programs for the quantitative electron beam X-ray-analysis of thick polished materials, thin-films, and particles. *Microbeam Analysis* 4:177–200.

Asimow P. D., Lin C., Bindi L., Ma C., Tschauner O., Hollister L. S., and Steinhardt P. J. 2016. Shock synthesis of quasicrystals with implications for their origin in asteroid collisions. *Proceedings of the National Academy of Sciences* 113:7077–7081.

Beck P., Gillet P., Gautron L., Daniel I., and El Goresy A. 2004. A new natural high-pressure (Na, Ca)-hexaluminosilicate $[(Ca_xNa_{1-x})Al_{3+x}Si_{3-x}O_{11}]$ in shocked Martian meteorites. *Earth and Planetary Science Letters* 219:1–12.

Beck P., Gillet P., El Goresy A., and Mostefaoui S. 2005. Timescales of shock processes in chondritic and Martian meteorites. *Nature* 435:1071–1074.

Beck P., Ferroir T., and Gillet P. 2007. Shock-induced compaction, melting, and entrapment of atmospheric gases in Martian meteorites. *Geophysical Research Letters* 34: L01203.

Binns R. A., Davis R. J., and Reed S. J. B. 1969. Ringwoodite, natural $(Mg,Fe)_2SiO_4$ spinel in the Tenham meteorite. *Nature* 221:943–944.

Boffa Ballaran T., Liu J., Dubrovinsky L. S., Caracas R., and Crichton W. 2009. High-pressure ferroelastic phase transition in aluminosilicate hollandite. *Physical Review B* 80:214104.

Bridges J. C. and Warren P. H. 2006. The SNC meteorites: Basaltic igneous processes on Mars. *Journal of the Geological Society, London* 163:229–251.

Byström A. and Byström A. M. 1950. The crystal structure of hollandite, the related manganese oxide minerals, and α-MnO_2. *Acta Crystallographica* 3:146–154.

Caracas R. and Boffa Ballaran T. 2010. Elasticity of (K,Na) $AlSi_3O_8$ hollandite from lattice dynamics calculations. *Physics of the Earth and Planetary Interiors* 181:21–26.

Chen M., El Goresy A., Frost D., and Gillet P. 2004. Melting experiments of a chondritic meteorite between 16 and 25 GPa: Implication for Na/K fractionation in a primitive chondritic Earth's mantle. *European Journal of Mineralogy* 16:201–211.

Deng L., Liu X., Liu H., and Dong J. 2010. High-pressure phase relations in the composition of albite $NaAlSi_3O_8$ constrained by an *ab initio* and quasi-harmonic Debye model, and their implications. *Earth and Planetary Science Letters* 298:427–433.

Dera P., Zhuravlev K., Prakapenka V., Rivers M. L., Finkelstein G. J., Grubor-Urosevic O., Tschauner O., Clark S. M., and Downs R. T. 2013. High pressure single-crystal micro X-ray diffraction analysis with GSE_ADA/RSV software. *High Pressure Research* 33:466–484.

Dowty E. 1987. Vibrational interactions of tetrahedra in silicate glasses and crystals. 3. Calculations on simple sodium and lithium silicates, thortveitite and rankinite. *Physics and Chemistry of Minerals* 14:542–552.

El Goresy A., Dera P., Sharp T. G., Prewitt C. T., Chen M., Dubrovinsky L., Wopenka B., Boctor N. Z., and Hemley R. J. 2008. Seifertite, a dense orthorhombic polymorph of silica from the Martian meteorites Shergotty and Zagami. *European Journal of Mineralogy* 20:523–528.

El Goresy A., Gillet P., Miyahara M., Ohtani E., Ozawa S., Beck P., and Montagnac G. 2013. Shock-induced deformation of shergottites: Shock-pressures and perturbations of magmatic ages on Mars. *Geochimica et Cosmochimica Acta* 101:233–262.

Ferroir T., Onozawa T., Yagi T., Merkel S., Miyajima N., Nishiyama N., Irifune T., and Kikegawa T. 2006. Equation of state and phase transition in $KAlSi_3O_8$ hollandite at high pressure. *American Mineralogist* 91:327–332.

Fritz J., Artemieva N., and Greshake A. 2005. Ejection of Martian meteorites. *Meteoritics & Planetary Science* 40:1393–1411.

Gillet P., Chen M., Dubrovinsky L., and El Goresy A. 2000. Natural $NaAlSi_3O_8$-hollandite in the shocked Sixiangkou meteorite. *Science* 287:1633–1636.

Harlow G. E. and Davies R. 2004. Status report on stability of K-rich phases at mantle conditions. *Lithos* 77:647–653.

Jackson I. and Ahrens T. J. 1979. Shock-wave compression of single-crystal forsterite. *Journal of Geophysical Research* 84:3039–3048.

Jeanloz R. 1980. Shock effects in olivine and implications for Hugoniot data. *Journal of Geophysical Research* 85:3163–3176.

Kawai K. and Tsuchiya T. 2013. First-principles study on the high-pressure phase transition and elasticity of $KAlSi_3O_8$ hollandite. *American Mineralogist* 98:207–218.

Kimura M., Chen M., Yoshida Y., El Goresy A., and Ohtani E. 2003. Back-transformation of high-pressure phases in a shock melt vein of an H-chondrite during atmospheric passage: Implications for the survival of high-pressure phases after decompression. *Earth and Planetary Science Letters* 217:141–150.

Kubo T., Kimura M., Kato T., Nishi M., Tominaga A., Kikegawa T., and Funakoshi K. 2009. Plagioclase breakdown as an indicator for shock conditions of meteorites. *Nature Geoscience* 3:41–45.

Langenhorst F. and Poirier J.-P. 2000. 'Eclogitic' minerals in a shocked basaltic meteorite. *Earth and Planetary Science Letters* 176:259–265.

Liebermann R. C. 1970. Velocity-density systematics for the olivine and spinel phases of Mg_2SiO_4-Fe_2SiO_4. *Journal of Geophysical Research* 75:4029–4034.

Liebermann R. C. 2014. The role of serendipity in my career in mineral physics: 1963–2013. *Physics of the Earth and Planetary Interiors* 228:307–323.

Liu L.-G. and El Goresy A. 2007. High-pressure phase transitions of the feldspars and further characterization of lingunite. *International Geology Review* 49:854–860.

Liu X. 2006. Phase relations in the system $KAlSi_3O_8$-$NaAlSi_3O_8$ at high pressure–high temperature conditions and their implication for the petrogenesis of lingunite. *Earth and Planetary Science Letters* 246:317–325.

Ma C. and Beckett J. R. 2017. A new type of tissintite, (Ca, Mg,Na,$\square_{0.14}$)(Al,Fe,Mg)Si_2O_6, in the Zagami Martian meteorite: A high-pressure clinopyroxene formed by shock (abstract #1639). 48th Lunar and Planetary Science Conference. CD-ROM.

Ma C. and Rossman G. R. 2008. Barioperovskite, $BaTiO_3$, a new mineral from the Benitoite Mine, California. *American Mineralogist* 93:154–157.

Ma C. and Rossman G. R. 2009. Tistarite, Ti_2O_3, a new refractory mineral from the Allende meteorite. *American Mineralogist* 94:841–844.

Ma C. and Tschauner O. 2017. Zagamiite, IMA 2015-022a. CNMNC Newsletter No. 36, April 2017, page 409. *Mineralogical Magazine* 81:403–409.

Ma C., Tschauner O., and Beckett J. R. 2014a. Liebermannite, IMA 2013-128. CNMNC Newsletter No. 20, June 2014, page 551. *Mineralogical Magazine* 78:549–558.

Ma C., Tschauner O., and Beckett J. R. 2014b. Liebermannite, $KAlSi_3O_8$-hollandite, a new high-pressure mineral formed by impact on Mars: An integrated SEM-EPMA-synchrotron diffraction investigation. Abstract MR11A-4307 presented at 2014 Fall Meeting, AGU, San Francisco, California, 15–19 December.

Ma C., Tschauner O., Beckett J. R., and Rossman G. R. 2015a. Liebermannite: A new potassic hollandite ($KAlSi_3O_8$) from the Zagami basaltic shergottite (abstract #1401). 46th Lunar and Planetary Science Conference. CD-ROM.

Ma C., Tschauner O., Beckett J. R., Liu Y., Rossman G. R., Zhuravlev K., Prakapenka V., Dera P., and Taylor L. A. 2015b. Tissintite, (Ca,Na,$\square$)$AlSi_2O_6$, a highly-defective, shock-induced, high-pressure clinopyroxene in the Tissint Martian meteorite. *Earth and Planetary Science Letters* 422:194–205.

Ma C., Tschauner O., Becket J. R., Liu Y., Rossman G. R., Sinogeikin S. V., Smith J. S., and Taylor L. A. 2016. Ahrensite, γ-Fe_2SiO_4, a new shock-metamorphic mineral from the Tissint meteorite: Implications for the Tissint shock event on Mars. *Geochimica et Cosmochimica Acta* 184:240–256.

Ma C., Tschauner O., and Beckett J. R. 2017. A new high-pressure calcium aluminosilicate ($CaAl_2Si_{3.5}O_{11}$) in Martian meteorites: Another after-life for plagioclase and connections to the CAS phase (abstract #1128). 48th Lunar and Planetary Science Conference. CD-ROM.

Malavergne V., Guyot F., Benzerara K., and Martinez I. 2001. Description of new shock-induced phases in the Shergotty, Zagami, Nakhla and Chassigny meteorites. *Meteoritics & Planetary Science* 36:1297–1305.

Mao H., Sundman B., Wang Z., and Saxena S. K. 2001. Volumetric properties and phase relations of silica—Thermodynamic assessment. *Journal of Alloys and Compounds* 327:253–262.

McCoy T. J., Taylor G. J., and Keil K. 1992. Zagami: Product of a two-stage magmatic history. *Geochimica et Cosmochimica Acta* 56:3571–3582.

McSween H. Y. 1994. What we have learned about Mars from SNC meteorites. *Meteoritics* 29:757–779.

Price G. D., Putnis A., Agrell S. O., and Smith D. G. W. 1983. Wadsleyite, natural β-$(Mg,Fe)_2SiO_4$ from the Peace River meteorite. *Canadian Mineralogist* 21:29–35.

Ringwood A. E., Reid A. F., and Wadsley A. D. 1967. High-pressure $KAlSi_3O_8$, an aluminosilicate with sixfold coordination. *Acta Crystallographica* 23:1093–1095.

Sharp T. G. and DeCarli P. S. 2006. Shock effects in meteorites. In *Meteorites and the early solar system II*, edited by Lauretta D. S. and McSween H. Y. Jr. Tucson, Arizona: The University of Arizona Press. pp. 653–677.

Sharp T. G., Lingemann C. M., Dupas C., and Stöffler D. 1997. Natural occurrence of $MgSiO_3$-ilmenite and evidence for $MgSiO_3$-perovskite in a shocked L chondrite. *Science* 277:352–355.

Sheldrick G. M. 2008a. A short history of SHELX. *Acta Crystallographica* A64:112–122.

Sheldrick G. M. 2008b. *CELL NOW program for unit cell determination*. Göttingen, Germany: University of Göttingen.

Smith J. V. and Mason B. 1970. Pyroxene-garnet transformation in Coorara meteorite. *Science* 168:832–833.

Stixrude L. and Lithgow-Bertelloni C. 2012. Geophysics of chemical heterogeneity in the mantle. *Annual Review of Earth and Planetary Sciences* 40:569–595.

Stöffler D., Keil K., and Scott E. R. D. 1991. Shock metamorphism of ordinary chondrites. *Geochimica et Cosmochimica Acta* 55:3845–3867.

Stolper E. and McSween H. Y. 1979. Petrology and origin of the shergottite meteorites. *Geochimica et Cosmochimica Acta* 43:1475–1498.

Tomioka N. and Fujino K. 1999. Akimotoite, $(Mg,Fe)SiO_3$, a new silicate mineral of the ilmenite group in the Tenham chondrite. *American Mineralogist* 84:267–271.

Tschauner O., Ma C., Beckett J. R., Prescher C., Prakapenka V. B., and Rossman G. R. 2014. Discovery of bridgmanite, the most abundant mineral in Earth, in a shocked meteorite. *Science* 346:1100–1102.

Walton E. L., Sharp T. G., Hu J., and Filiberto J. 2014. Heterogeneous mineral assemblages in Martian meteorite Tissint as a result of a recent small impact event on Mars. *Geochimica et Cosmochimica Acta* 140:334–348.

Yagi A., Suzuki T., and Akaogi M. 1994. High pressure transitions in the system $KAlSi_3O_8$-$NaAlSi_3O_8$. *Physics and Chemistry of Minerals* 21:12–17.

Yamada H., Matsui Y., and Ito E. 1984. Crystal-chemical characterization of $KAlSi_3O_8$ with the hollandite structure. *Mineralogical Journal* 12:29–34.

Zhang J., Ko J., Hazen R. M., and Prewitt C. T. 1993. High-pressure crystal chemistry of $KAlSi_3O_8$ hollandite. *American Mineralogist* 78:493–499.